



Climate change may increase landslide frequency despite generally drier conditions in the Mediterranean area

Daniel Camilo Roman Quintero^{1,2}, Ruud van der Ent², Thom Bogaard², Roberto Greco¹

¹Università degli Studi della Campania “Luigi Vanvitelli”, Dipartimento di Ingegneria, Aversa, Italy

²Department of Water Management, Delft University of Technology, Delft, the Netherlands

Correspondence to: Daniel Camilo Roman Quintero (dromanquintero@tudelft.nl)

Abstract. This study presents a methodological framework to investigate the impacts of climate change on rainfall-triggered landslides at the subregional scale. Focusing on a ~170 km² area in the Partenio Mountains in southern Italy, we employed regional rainfall projections (CORDEX) under moderate (RCP4.5) and high (RCP8.5) emission scenarios for 2006–2070. Rainfall data were bias-corrected with observations from 2006–2023 and benchmarked against a synthetic dataset generated through stochastic reproduction of currently observed conditions. Physically based simulations of hydrological processes, coupled with slope stability analyses that account for unsaturated soil conditions, enabled event-by-event identification of landslides throughout the period. Statistical comparisons between scenarios were conducted across three rainfall homogeneous subregions. Results show a general tendency toward drier soil conditions, consistent with regional-scale climate studies, but with increasing rainfall variability across subregions. Despite this drying trend, projections indicate a significant rise in landslide occurrence, with a faster increase under RCP4.5 when compared to RCP8.5. This counterintuitive outcome reflects shifts in rainfall dynamics: under RCP8.5, landslides are mainly linked to more intense triggering rainfall, while under RCP4.5 they result from a combination of wetter antecedent conditions and more intense early-peak rainfall events. These findings emphasize the critical role of antecedent soil moisture in landslide initiation by showing its stable influence on landslide occurrence despite the rapid evolution of climate change. Overall, the methodology provides a transferable framework to assess local climate change impacts on geohazards by integrating bias-corrected climate projections with physically based hydrological–geomechanical modeling.

Keywords: Rainfall-triggered landslides; climate change; bias correction; systemic trend evolution;



32 **1. Introduction**

33 Understanding how the evolving climatic drivers regulate landslide occurrence is essential for
34 adapting hazard management practices at local scales in landslide-prone regions, within a climate
35 change context. Rainfall-triggered landslides are a complex natural hazard, resulting from non-
36 linear interactions among meteorological forcing, transient subsurface hydrology, and the
37 mechanical properties of slopes. Key triggering mechanisms are caused by infiltration of rainfall
38 into the soil and even its interaction with underlying bedrock conditions, elevating pore water
39 pressure, reducing effective stress, and weakening shear strength along potential failure planes.
40 These mechanical responses are determined by rainfall characteristics (e.g., intensity, duration,
41 accumulation) and strongly influenced by hydrological conditions, determining soil water content
42 conditions, which are shaped by preceding hydrological processes. The "filling-storing-draining"
43 concept offers a valuable framework for interpreting the temporal evolution of pore pressures,
44 describing how slope materials sequentially absorb, retain, and discharge infiltrated water
45 (Bogaard and Greco, 2016). Understanding these processes is essential for assessing slope stability
46 under dynamic climatic conditions, influenced by atmospheric dynamics and climate change.
47 The influence of climate change on rainfall patterns is increasingly evident in observational records
48 and consistently projected by climate models for the coming decades (Avino et al., 2024; Capozzi
49 et al., 2023; Gründemann et al., 2022). Ensembles of high-resolution projections, such as those
50 developed under initiatives like EURO-CORDEX, provide detailed insights into expected future
51 climatic conditions, often indicating significant alterations in precipitation characteristics across
52 Europe and other regions by the end of the 21st century (Jacob et al., 2014). However, raw outputs
53 from Regional Climate Models (RCMs) often contain magnitude biases, leading to discrepancies
54 in key statistical properties when compared to detailed observations in rain gauges. Since
55 hydrological and slope stability models are sensitive to the magnitude and variability of
56 meteorological inputs, bias correction is essential for reliable climate impact assessments on local
57 and regional scales (Ehret et al., 2012; Teutschbein and Seibert, 2012). Parametric quantile
58 matching (QM), as applied in the ISIMIP framework (Davie et al., 2013), adjusts simulated
59 distributions to match observed ones using additive or multiplicative corrections, depending on the
60 variable type. Advanced methods such as the Multivariate Recursive Nested Bias Correction
61 (MRNBC) extend QM to preserve inter-variable correlations and temporal consistency (Kim et
62 al., 2023). For capturing extremes, the Quantile Matching for Extremes (QME) method enhances



63 resolution in distribution tails, essential for landslide-triggering rainfall (Vogel et al., 2023). By
64 ensuring more realistic inputs, bias correction improves the representation of hydrological
65 processes under climate change, particularly those influencing slope saturation and landslide
66 occurrence (Peter et al., 2024).

67 Addressing the inherent complexities and uncertainties in predicting landslide occurrence,
68 especially over local areas (i.e. between 10^2 km² and 10^3 km²) under future conditions, necessitates
69 innovative approaches. Physically based synthetic data generation has emerged as a powerful tool
70 in this domain, enabling researchers to overcome limitations associated with sparse observational
71 records and to explore slope responses across a wide spectrum of potential hydro-meteorological
72 conditions (Roman Quintero et al., 2023; Roman Quintero, et al., 2024). By simulating extensive
73 datasets, often employing stochastic models for rainfall (e.g., Peres and Cancelliere, 2014, 2016;
74 Rodriguez-Iturbe et al., 1987a) coupled with hydrological and slope stability models, it becomes
75 possible to systematically investigate the influence of various factors and estimate landslide
76 probabilities under diverse conditions. This involves differentiating between the influence of
77 relatively static landscape attributes (e.g., topography, soil type distribution, geology, land cover)
78 and highly dynamic factors (e.g., rainfall forcing, evolving soil moisture fields) (Bozzolan et al.,
79 2025; Fang et al., 2024). Such methodologies are particularly pertinent for assessing the potential
80 impacts of climate change, as they allow for the explicit incorporation of altered dynamic drivers
81 (e.g., modified rainfall inputs derived from climate projections) to evaluate consequent shifts in
82 slope stability and landslide likelihood at local scales (Gariano and Guzzetti, 2016; Stoffel et al.,
83 2014).

84 Despite extensive research on the effects of climate change on hydrometeorological hazards, the
85 systemic understanding of how evolving climate conditions translate into changes in landslide
86 occurrence remains limited, particularly at the subregional scale. Most existing studies rely on
87 empirical correlations between rainfall trends and landslide records, demonstrating with data
88 records the observed effects of climate change on this geohazards, but often overlooking the
89 physically based processes that link climate forcing, subsurface hydrology, and slope stability
90 (Crozier, 2010; Gariano et al., 2015; Semnani et al., 2025; Stoffel et al., 2014). In particular, there
91 is a lack of systematic investigation into how projected changes in rainfall regimes, characterized
92 by increased temporal variability and altered antecedent moisture conditions, may influence the
93 triggering mechanisms of rainfall-induced landslides. Moreover, while ensemble climate



94 projections are widely used to assess future climatic patterns, their large variability can obscure
95 the understanding of how climate change affects highly non-linear processes such as slope
96 response to precipitation; an aspect that has been rarely explored through process-based modeling
97 frameworks (Buonacera et al., 2025; Crozier, 2010). Addressing this knowledge gap requires
98 integrating bias-corrected regional climate projections with coupled hydrological–geomechanical
99 simulations to evaluate how subsurface processes respond to changing climatic forcing and to
100 quantify the potential for increased landslide occurrence despite any overall rainfall trend.
101 This study aims to propose a novel methodology to quantitatively assess the local impacts of
102 regional climate change on rainfall-triggered landslide occurrence. The methodology, applied
103 within a study area, uses a coupled physically based hydrological and slope stability modeling
104 framework driven by bias-corrected RCM outputs under different emission scenarios, and
105 incorporates current climate conditions for benchmarking. We analyze the complex interactions
106 between future climate scenarios, local-scale hydrological responses, and slope stability dynamics.
107 The core objective is to address two fundamental research questions regarding future landslide
108 probability of occurrence in subregional scales: (1) How is rainfall expected to change in terms of
109 event magnitude, duration and temporal distribution? And (2) How will those changes affect future
110 landslide occurrence? The outcomes of this research are expected to provide insights into landslide
111 probability quantification, susceptibility, hazard and landslide risk assessments under changing
112 climate conditions.
113



2. Materials and methods

To reveal the impact of climate change on the occurrence of rainfall-triggered landslides, this study uses a physically based modelling framework. Figure 1 illustrates the conceptual framework linking climate forcing, hydrological processes, and slope stability assessment from a dynamic perspective. At the highest level, socio-economic development (SD) drives greenhouse gas emissions, represented by the Representative Concentration Pathways (RCs), which in turn influence global and regional climate conditions. These forcings affect temperature (T) and atmospheric dynamics (AD), which jointly control precipitation (P) regimes and evaporation–evapotranspiration (E–ET) processes.

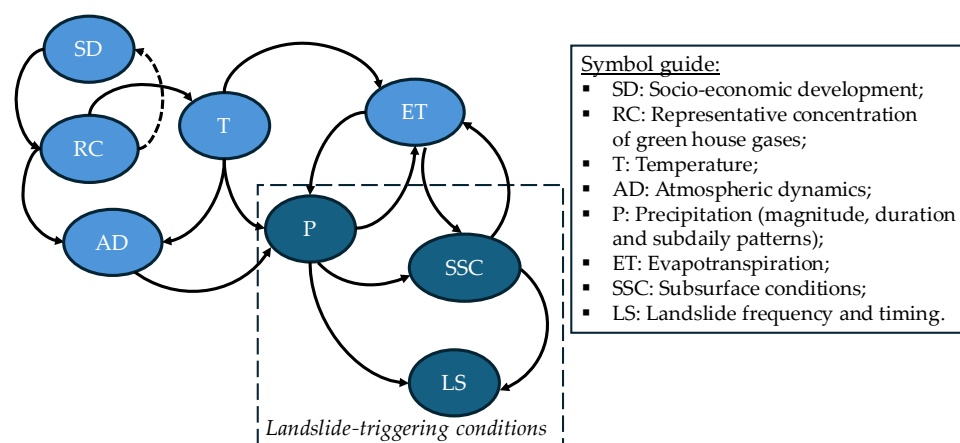


Figure 1. Influence diagram displaying the methodological framework proposed in the study.

The meteorological forcing (P and ET) plays a central role, acting as the primary external driver of landslide-triggering conditions. Precipitation frequency, magnitude, duration, and sub-daily distribution determine the temporal evolution of subsurface conditions (SSC), such as soil moisture and pore water pressure. These conditions are critical in setting the proneness of a slope to failure. Simultaneously, E–ET regulates water loss from the soil–plant–atmosphere system, modulating SSC and influencing the balance between infiltration and drainage. Ultimately, landslide frequency and timing (LS) emerge as the response variable of this coupled system, reflecting the combined effects of precipitation forcing and antecedent subsurface conditions. Rainfall infiltration and slope stability were simulated with a physical based numerical model (see section 2.2).

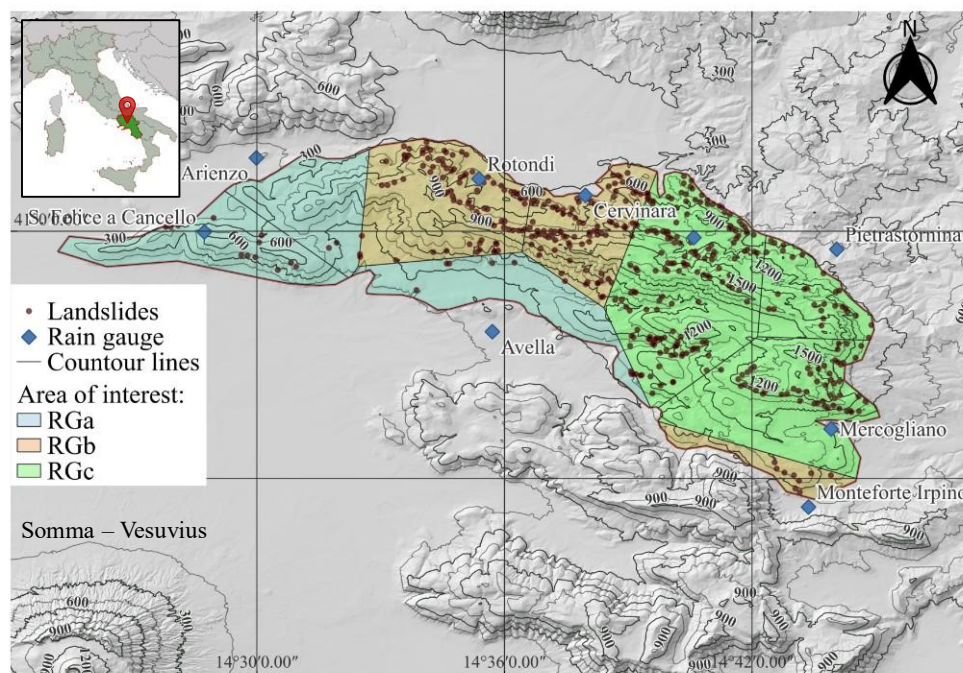


134 2.1. Study area

135 This study investigates a ~170 km² landslide-prone area within the Partenio Massif, Campania
 136 Region, southern Italy (Figure 2). Located in the southern Apennines, this geomorphologically
 137 homogeneous subregion is prone to shallow landslides and debris flows.

138 The area has a typical Mediterranean climate, with average annual precipitation ranging between
 139 1000 mm and 2000 mm. Total potential evapotranspiration ranges from 700 mm to 800 mm (at
 140 400–750 m a.s.l.), and mean daily temperatures vary from approximately -4.0°C in the cold season
 141 to 30°C in the warm season.

142 The area is monitored by a network of nine meteorological stations managed by the Italian Civil
 143 Protection Agency. These stations, operational since 2003–2004, are equipped with rain gauges
 144 providing observed sub daily rainfall data, which was used in the present study.



145
 146 *Figure 2. Landslide-prone area in the Partenio Mountains, Campania Region, southern Italy, and the three subregional groups*
 147 *RGa (blue), RGb (orange), and RGc (green), characterized by similar precipitation characteristics. Landslide data are taken from*
 148 *the Inventario dei Fenomeni Franosi d'Italia (Iadanza et al., 2021).*

149 The rainfall stations were categorized into three distinct sub-regional groups (RGa, RGb and RGc)
 150 based on both their spatial distribution and the statistical similarity of the rainfall events. Pairwise
 151 Kolmogorov–Smirnov (KS) tests were conducted at a 5% significance level ($\alpha = 0.05$).



152 In fact, according to observed rainfall, mean annual rainfall increases from the least rainy group,
 153 RGa (~1050 mm/year), to the intermediate group, RGb (~1600 mm/year), and finally to the rainiest
 154 group, RGc (~1820 mm/year).

155 Geomorphologically, the Partenio Mountains feature steep slopes covered by a thin mantle of
 156 coarse-grained volcanic soils (pyroclastic deposits), ranging from less than 1 m on steep parts to
 157 over 6 m in flatter areas (Del Soldato et al., 2018; De Vita and Nappi, 2013). These soils overlie a
 158 fractured and karstic limestone bedrock. Due to their gentle airfall deposition, the soils have high
 159 porosities (up to 0.7), making them highly permeable in saturated conditions, yet they maintain a
 160 high shear strength with friction angles around 38° (Picarelli et al., 2006).

161 This combination of pyroclastic deposits and fractured limestone creates a hydrogeological setting
 162 contributing to rapid pore pressure responses. The uppermost highly weathered part of the
 163 limestone bedrock, known as epikarst (Celico et al., 2010; Williams, 2008), hosts a perched aquifer
 164 during wet seasons. This aquifer exchanges water with the unsaturated soil mantle, a process that
 165 becomes evident in mid-winter when several ephemeral springs feed local streams (Roman
 166 Quintero et al., 2023).

167 Previous investigations have shown that while the landslide-prone area is relatively uniform,
 168 landslide initiation is highly sensitive to specific rainfall thresholds and pre-existing soil wetness
 169 states. This highlights the importance of integrating both short-term rainfall events and long-term
 170 hydrological conditions in modeling frameworks (Marino et al., 2020a; Picarelli et al., 2006;
 171 Roman Quintero et al., 2025; Del Soldato et al., 2018; De Vita and Nappi, 2013).

172 **2.2. Numerical Simulation of Hillslope Hydrological Processes and Stability Analysis**

173 The hydrological processes governing the water storing in the sloping pyroclastic soil deposits,
 174 despite the rainfall itself, have been proved to be linked to the infiltration capacity of the soil
 175 (Greco et al., 2023; Roman Quintero et al., 2023). Figure 3 represents the main physical processes
 176 affecting the water balance of slopes in the area, including shallow surface processes as rainfall
 177 infiltration and evapotranspiration, and deeper ones as water leakage to the perched aquifer and
 178 drainage to deeper systems.

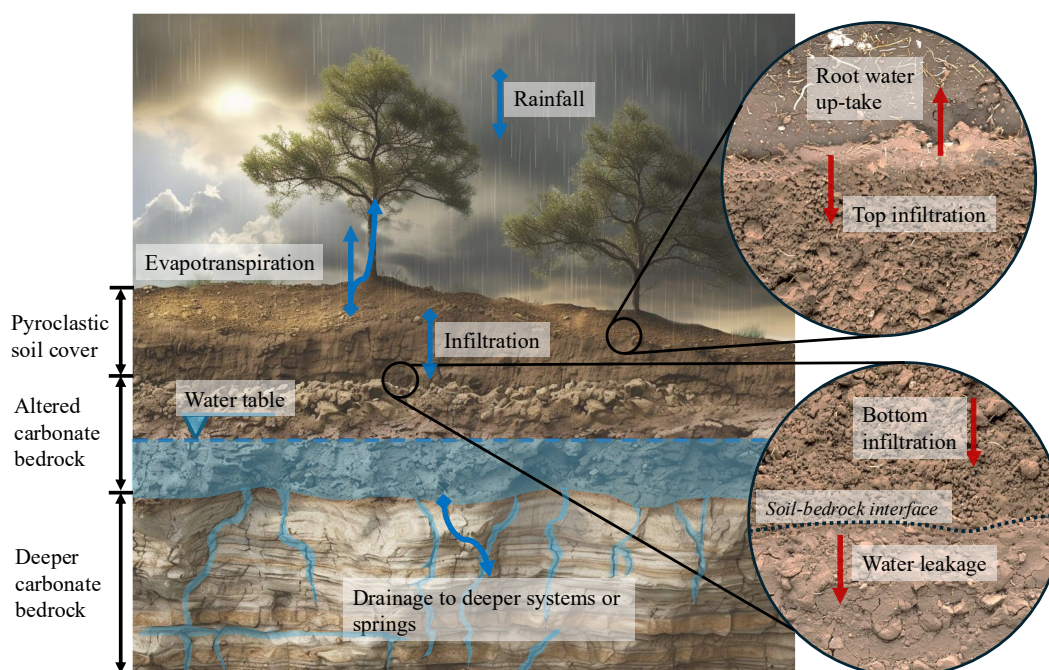
179 A previously developed and validated physically based model incorporating dominant
 180 hydrological processes at the hillslope scale was implemented to characterize the transient water
 181 dynamics in landslide-prone slopes within the study area (Greco et al., 2013, 2018; Marino et al.,
 182 2021; Marino, Peres, et al., 2020; Roman Quintero, et al., 2024). The modeling framework



183 numerically solves the 1D Richards equation for unsaturated flow through the pyroclastic soil
 184 matrix, coupled with a bucket-type groundwater representation of the Epikarst aquifer, connected
 185 to the soil deposits through its lower boundary condition.

186 The pyroclastic soils of the area exhibit high porosity ($\theta \sim 0.65-0.7$), resulting in saturated
 187 hydraulic conductivity values ranging between about 10^{-4} m/s and 10^{-5} m/s. These hydraulic
 188 properties renders very unlikely the overland runoff generation, when compared with the observed
 189 maximum hourly rainfall intensities, always less than 70 mm/h, justifying its exclusion from the
 190 simulations (Picarelli et al., 2020; Roman Quintero et al., 2025).

191 Simulations were conducted by running the model across different rainfall time series. While the
 192 meteorological forcing imposed by rainfall will be explained in detail later, we used both time
 193 series representing climate change scenarios and current climate conditions. In turn, the potential
 194 evapotranspiration (PET) was assumed to variate on a monthly basis and was estimated with the
 195 Thornthwaite formula (Marino, et al., 2020).



196
 197 *Figure 3. Main hydrological processes affecting the water cycle and water stored in the pyroclastic soil cover affecting slope*
 198 *stability in the landslide-prone study area.*

199 For simplicity, under all projected conditions, PET was assumed to be equivalent to that of the
 200 observed period, ranging between 4–5 mm/day in summer and less than 1 mm/day in winter. This



assumption is supported by two main reasons. First, although evapotranspiration influences soil moisture seasonally, its role in slope instability is likely minor because rainfall-triggered landslides typically occur during wet and cold periods when PET is only 0–2 mm/day compared with the ~300 mm over 2–3 days of triggering rainfall (Greco et al., 2021). Furthermore, while PET is projected to increase slightly (mainly in summer and only marginally in winter) its relevance for slope stability remains limited, especially because actual ET is constrained by soil-water availability and no major vegetation changes are expected that would enhance ET in proportion to PET.

Landslide-prone slopes associated with the most impactful landslides in the study area share similar morphological characteristics: a pyroclastic soil cover approximately 2 m deep on slopes with inclinations of about 40° (Greco et al., 2021). These representative conditions were used for all simulations and slope stability was assessed by calculating the factor of safety (FS) at each simulated timestep, accounting for unsaturated material conditions. The detailed property values and further model details can be found in Roman Quintero et al. (2025).

2.3. Projected rainfall under current and climate change conditions

This study uses rainfall projections to define three data ensembles representing both current and climate change conditions. For the currently observed climate, the Neyman–Scott Rectangular Pulse (NSRP) stochastic rainfall model was used to generate nine synthetic hourly precipitation time series at each observation point (rain gauges), each spanning 65 years and based on observed data, resulting in a total of 81 time series. This ensemble, referred to here as CTRL, covers the simulated period from 2006 to 2070 and serves as the reference for comparison.

Specifically, The NSRP model conceptualizes rainfall as a sequence of storm clusters, each composed of rectangular pulse cells with randomly distributed start times (Rodriguez-Iturbe et al. 1987; Cowpertwait et al. 1996). In this way, the duration of each pulse represents the lifetime of a rain cell, while the pulse height corresponds to rainfall intensity. When multiple cells overlap in time, their intensities are cumulatively summed to determine the total precipitation rate. Calibration of the NSRP model for the study area has been presented in previous studies and was performed using the method of moments (Peres and Cancelliere, 2014; Roman Quintero et al., 2023).

Climate change rainfall projections were extracted from regional climate studies from two sources: the EURO-CORDEX initiative, produced by several multinational climate modeling centers, and



the Very High Resolution Climate Projections for Italy (VHR-PRO_IT), produced by the Euro-Mediterranean Center on Climate Change (CMCC Foundation). In both cases, the climate projection simulations start from 2006. The CORDEX initiative represents a set of experiments developed under an international framework involving 26 climate modeling centers worldwide, contributing 11 regional climate model simulations. The data used in this study correspond to downscaled CMIP5 global simulations (at ~12.5 km horizontal resolution, with 3h temporal resolution), incorporating Representative Concentration Pathways (RCPs) (Moss et al., 2010; Taylor et al., 2012; van Vuuren et al., 2011). RCPs are a set of scenarios that integrate greenhouse gas emissions, concentrations, and land-use trajectories with socio-economic developments. Here, two scenarios were analyzed: RCP4.5 (including mitigation measures) and RCP8.5 (very high emissions, often termed "business as usual") (van Vuuren et al., 2011). A total of 9 ensemble members were used here for RCP4.5 and 9 for RCP8.5 scenarios.

The second source consists of the VHR-PRO_IT dataset, which provides an additional ensemble member produced with the COSMO-CLM model at ~2.2 km horizontal resolution and hourly temporal resolution. This initiative largely follows the CORDEX framework (from data management to experimental design), making it suitable for inclusion in the analysis. Specifically, VHR-PRO_IT downscales an existing regional dataset for Italy (Italy8km-CM; (Bucchignani et al., 2016)), which itself downscales the global forcing from CMIP5 simulations from different RCP scenarios.

In summary, we used a total of 9 ensemble members for RCP4.5 and 9 for RCP8.5 climate change scenarios, resulting in 81 study units (time series) at the observation points (rain gauge locations). Temperature projections from the same scenarios were also displayed to illustrate the co-evolution of the studied variables with temperature rise, although they were not directly used in subsequent calculations. Rainfall data from both sources were further spatially downscaled and bias-corrected. The selected temporal resolution was 3 hours, constrained by the EURO-CORDEX dataset. Simulations of hillslope hydrological processes and slope stability were then performed from 2006 (the standard baseline year for climate change projections) to 2070, limited by data availability in the VHR-PRO_IT dataset.

2.3.1. Statistical Bias Correction of rainfall projections

Since this study focuses on a local area in Partenio mountains of southern Italy, and the studied process is affected by extreme rainfall, we applied the Quantile Matching for Extremes (QME)



method to further downscale rainfall to the observation points (rain gauge locations), and bias-correct climate model projections against observed data. The method was applied with data recorded from the stations between 2006 and 2023.

QME is widely used in meteorological applications and is particularly well-suited for studies where extreme rainfall events are a key focus (Peter et al., 2024). The procedure utilized here is fundamentally based on bias-correction procedure proposed by (Dowdy, 2023), enhanced by adding a previous correction step matching the number of rainy cells of modeled rainfall data, with the observed values. For a detailed view of the algorithm, visit the repository accompanying this study (Roman Quintero, 2025).

Before applying QME, the model and observed rainfall data were scaled to make them directly comparable. This normalization step ensures that both datasets share a common reference range, accounting for the rain gauge resolution (0.2 mm) and the maximum observed or simulated rainfall values for each case.

The bias correction was then carried out quantile by quantile. First, we estimated the empirical cumulative distribution functions (CDFs) of both the observed and modeled rainfall data. Each modeled quantile was then matched to its corresponding observed quantile, using both forward and backward scans to minimize mismatches. The final bias-corrected value for each quantile was obtained by averaging the results from these two scans.

To better capture the behavior of extreme events (a key objective of this study) an additional correction was applied to the upper tail of the rainfall distribution (above the 95th percentile). For this step, we compared the mean rainfall values of the observed and modeled datasets in this extreme range and adjusted the modeled values accordingly. When the extreme-value correction produced a larger adjustment than the standard quantile matching, the extreme correction was retained.

Finally, the resulting bias-correction values were applied to the scaled model rainfall data, producing a dataset with magnitudes statistically consistent with local observations while preserving the distribution of extreme events.

The bias-corrected rainfall projections were aggregated into discrete rainfall events. An event was defined as a period with at least 2 mm rainfall, preceded and followed by at least 24 consecutive hours of not exceeding 2 mm of cumulative rainfall. This event definition enables



isolation of individual storm impacts on hydrological response interesting landslide events,
 particularly in the uppermost part of the pyroclastic soil cover (Roman Quintero et al., 2023).

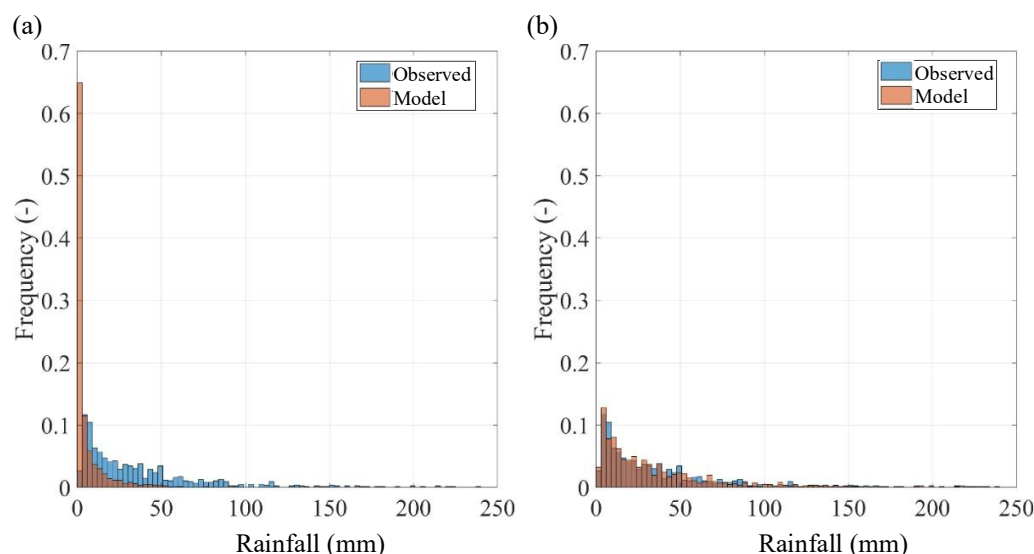


Figure 4. Frequency data distributions of the Observed and Modeled Rainfall Events from the VHR-PRO_IT dataset for the Cervinara station in the observation period: (a) before the application of the bias-correction procedure and (b) after the application of the bias-correction procedure.

Event separation served two primary purposes: (1) to delineate distinct wet and dry periods within the analysis timeframe; and (2) to enable characterization of event-specific properties (magnitude, intensity and discretization of extreme rainfall events) and their impacts on slope stability. Figure 4 show the complete data distributions of rainfall events in both modeled and observed datasets for Cervinara station. Figure 4(a) and Figure 4(b) present the model data distribution before and after applying the bias-correction, respectively.

2.3.2. Trend analysis of projected magnitudes

Trend analysis was conducted in two stages: (1) exploring overall changes in rainfall and subsurface characteristics without distinguishing between landslide-triggering and non-triggering events, and (2) analyzing only landslide-triggering events.

Rainfall magnitude, duration, event temporal patterns, and volumetric water content prior to each rainfall event were analyzed on a seasonal basis to identify trends during critical months that contribute to landslide-prone soil conditions. Specifically, mean seasonal projected quantities, along with their standard errors, were analyzed for different periods to capture typical seasonal



313 conditions: Autumn from September to October (SON), marking the onset of the hydrological
 314 year; Winter from December to February (DJF), representing an intermediate wet and cold period;
 315 Spring conditions from March to May (MAM), preceding the onset of dryer conditions; and (d)
 316 Summer from June to August (JJA), indicating the warmest and driest conditions before the end
 317 of the hydrological year.

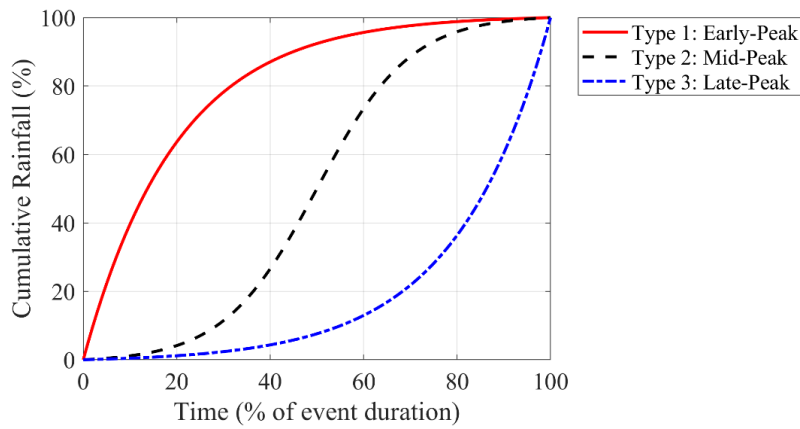
318 For the trend analysis we applied a time series decomposition to the projected rainfall data from
 319 each climate model at every rain gauge observation point. For this purpose, we used Singular
 320 Spectrum Analysis (SSA), a non-parametric technique that separates a time series into meaningful
 321 components without assuming a predefined functional form (Golyandina and Zhigljavsky, 2013).
 322 The SSA process begins by reconstructing each rainfall time series into a form that preserves its
 323 temporal structure while enabling a detailed examination of its underlying patterns. A 30-year
 324 sliding time window was used to capture long-term variability. This transformation allows the data
 325 to be expressed as a combination of components that represent different sources of variability.

326 The transformed data were then analyzed to identify the most important components, i.e. those
 327 that contribute most strongly to the overall variability of the series. The leading components, which
 328 describe slow and persistent changes, were interpreted as the trend signal. Their selection was
 329 guided by their dominant contribution to the total variability and their smooth, monotonic
 330 evolution over time. Each identified trend was cross-checked against expectations for long-term
 331 variability within the original time series to ensure consistency. The remaining components, which
 332 represent progressively smaller contributions, typically correspond to oscillatory patterns (such as
 333 seasonal or interannual cycles) or high-frequency noise. Since this study focuses on long-term
 334 rainfall changes, these shorter-term fluctuations were not analyzed further. Finally, the selected
 335 components were transformed back into the time domain to produce a smoothed representation of
 336 the underlying trend. This approach is robust to noise and missing data, making it particularly well
 337 suited for detecting long-term signals in climate projections.

338 Rainfall hyetograph is known to be related to slope instabilities (D’Odorico et al., 2005).
 339 Specifically, the effect of rainfall event temporal patterns was assessed by classifying rain events
 340 according to their maximum peak intensity (Wu et al., 2006). Figure 5 presents a schematic view
 341 of this rainfall-type characterization, according to hyetograph shape. Type 1 (“early-peak”) events
 342 concentrate most of the rainfall during the initial phase of the event, with the cumulative total
 343 reaching 50% of the event rainfall within the first 40% of its duration. Type 2 (“mid-peak”) events



344 exhibit a near-uniform or Gaussian temporal distribution, with cumulative rainfall reaching 50%
 345 approximately midway through the event (between 40% and 60% of its duration). Type 3 (“late-
 346 peak”) events release most of the rainfall toward the end of the event, with cumulative rainfall
 347 reaching 50% only after 60% of the duration has elapsed. This classification helps describe the
 348 internal temporal structure of rainfall events beyond total depth and duration. More specifically,
 349 hyetographs are analyzed for both the triggering rainfall event and the antecedent rainfall event;
 350 that is, the one occurring immediately before the triggering event.



351

352 *Figure 5. Schematic representation of rainfall event types based on the temporal distribution of cumulative rainfall. The x-axis*
 353 *represents the percentage of event duration, while the y-axis indicates the cumulative percentage of rainfall.*

354 **2.4. Analysis of the influence of future climate scenarios on landslide occurrence**

355 Landslide events were identified within the simulations once the factor of safety (FS) from slope
 356 stability analyses passed from $FS > 1.1$ to $FS \leq 1.1$, similarly as described in Roman Quintero et
 357 al. (2025). The landslide occurrence was studied using two metrics. First, the yearly ensemble
 358 landslide frequency λ_{LS} , defined in equation (1).

$$\lambda_{LS}(t) = \frac{1}{N_{EM}} \sum_{i=1}^{N_{EM}} N_{LS,i}(t) \quad (1)$$

359 where $N_{LS,i}(t)$ is the number of landslides identified in year t for ensemble member i , and N_{EM} is
 360 the number of ensemble members.

361 λ_{LS} was further analyzed in terms of anomalies ($\Delta\lambda_{LS}$), defined as the difference between the yearly
 362 $\Delta\lambda_{LS}$ values and the value at the beginning of the study period (i.e., 2006).



363 Second, the rainfall-triggered landslide marginal probability (P_{LS}) was estimated as the number of
 364 landslide events divided by the number of rain events, both occurring over a 20-year period at each
 365 rain gauge station, and computed as:

$$P_{LS} = \frac{N_{LS,20y}}{N_{RE,20y}} \quad (2)$$

366 where $N_{LS,20y}$ is the number of landslides identified over a 20-year period, and $N_{RE,20y}$ is the
 367 number of rainfall events within the same period. In this study, P_{LS} was evaluated for the periods
 368 2006–2026 and 2050–2070.

369 P_{LS} was further analyzed in terms of the relative change in landslide probability (δP_{LS}) during
 370 2050–2070 with respect to 2006–2026.

371 Therefore, the proposed experimental procedure investigates changes in landslide occurrence by
 372 accounting for two critical factors influencing the incidence of rainfall-triggered landslides: (i) the
 373 effects of rainfall changes projected under different climate scenarios, and (ii) the local rainfall
 374 variability within the study area.

375 The experiment was structured as a 3×3 factorial design combining three climate projection
 376 scenarios (RCP 8.5, RCP 4.5, and CTRL) with three groups of rain gauges representing distinct
 377 spatial sectors of the study area. Each combination included 27 study units, corresponding to
 378 landslide time series derived from the climate ensembles, ensuring statistically consistent results
 379 with a test power ≥ 0.9 (Erdfelder et al., 2009).

380 The resulting data were analyzed using the Analysis of Variance of Aligned Rank Transformation
 381 (ANOVA-ART; Wobbrock et al., 2011) to evaluate the influence of climate change and the spatial
 382 and temporal variability of rainfall projections on landslide occurrence. When the ANOVA-ART
 383 indicated statistically significant results, post-hoc tests of Estimated Marginal Means (EMMs)
 384 were performed to identify significant pairwise differences between climate scenarios and spatial
 385 rainfall groups (Lenth, 2025; Searle et al., 1980).

386

387 **3. Results**

388 **3.1. Projected changes in rainfall and soil antecedent conditions**

389 Figure 6 presents the seasonal median values of the trend components for total rainfall, duration,
 390 and antecedent volumetric water content, respectively for the different scenarios. Figure 6(a)
 391 presents the time series of anomalies for total rainfall per event during SON, showing opposite



trends: negative for the RCP4.5 scenario and positive for the RCP8.5 scenario. Figure 6(d) shows a positive trend for RCP8.5, while conditions remain relatively stable under RCP4.5 during DJF. Figure 6(g) shows a slightly negative trend in both scenarios during MAM, similar to Figure 6(j) during JJA. In all cases, CTRL exhibits relatively stable conditions. Similarly, Figure 6(b) presents the anomalies for rainfall event duration, showing a negative trend for RCP4.5 and stable conditions for RCP8.5 in SON. Figure 6(e) shows stable conditions for RCP8.5, but a positive trend for RCP4.5. Figure 6(h, k) show a negative trend for both scenarios during MAM and JJA, respectively. In contrast, CTRL exhibits relatively stable conditions, excepting SON.

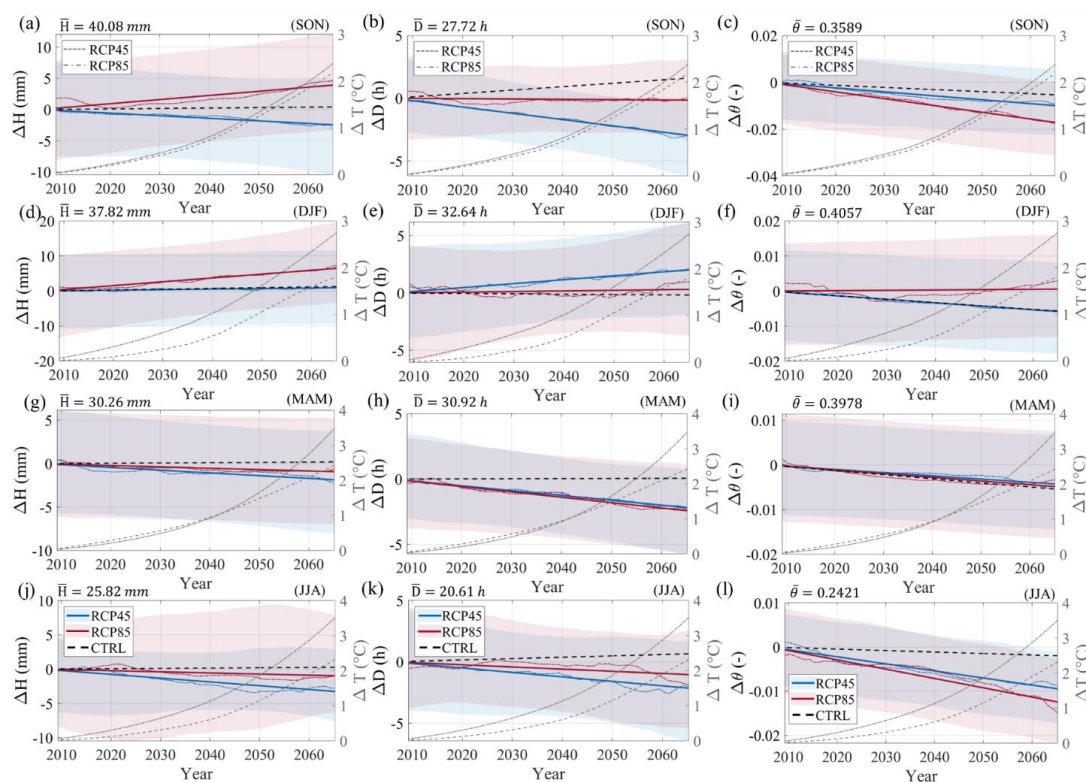


Figure 6. Anomalies in the trend of investigated quantities (dashed lines) and its linear interpolation (solid lines) for: (a, d, g, j) total event rainfall (ΔH), (b, e, h, k) duration (ΔD), and antecedent volumetric water content ($\Delta \theta$), along with projected temperature shift (ΔT) in the study area on a seasonal basis: (a-c) September; October, November (SON); (d-f) December, January, February (DJF); (g-i) March, April, May (MAM); (j-l) June, July, August (JJA). Average magnitudes at the beginning of the period are reported in the top-left corner as reference.

Likewise, Figure 6(c) displays a negative trend in anomalies on volumetric water content prior to rainfall initiation under both the RCP4.5 and RCP8.5 scenarios during SON. Figure 6(f) shows



409 stable conditions for RCP8.5 but a negative trend for RCP4.5 during DJF. Figure 6(i, l) show a
 410 negative trend in both climate change scenarios. In this case, CTRL also shows a negative trend,
 411 although it is generally less pronounced.

412 Figure 7 presents a map dividing the area according to the three groups established in section 2.4:
 413 Group a – RGa, Group b – RGb and Group c – RGc. The geographical representation, constructed
 414 with Voronoi polygons, represent areas where total rainfall per event are statistically similar.
 415 Moreover, in the inner tables of the same figure, it displays the direction of the trend in scenarios
 416 RCP4.5 and RCP8.5 and the percentage of agreement amongst the ensemble members in brackets
 417 (e.g. +(81 %) for total rainfall trend in SON, for group b).

418 Furthermore, Figure 7 shows the climate change trends and their interaction with spatial variability
 419 across the study area, together with model spread among ensemble members. Overall, the entire
 420 area exhibits a projected tendency toward smaller and shorter rain events and drier antecedent
 421 conditions, reflected in negative trends for event rainfall, duration, and antecedent volumetric
 422 water content.

423 However, both climate change scenarios indicate wetter conditions in DJF, with increases in H and
 424 D. Projected trends highlight a marked seasonal contrast, with wetter winters (DJF) and
 425 progressively drier spring–summer periods (MAM–JJA). Under RCP4.5, H and D generally
 426 decrease in SON, MAM, and JJA but increase in DJF, while θ consistently declines across all
 427 seasons. RCP8.5 amplifies these patterns, producing stronger wetting in SON and DJF (up to +73%
 428 agreement for H) and more severe drying in MAM (θ down to –97%) and JJA. Spatially, Group c
 429 exhibits the strongest wetting signal in SON and DJF, whereas Groups a and b show more
 430 pronounced drying in MAM. These results suggest an intensification of seasonal contrasts, with
 431 stronger storms entering the hydrological year, wetter soils but becoming progressively drier
 432 toward summer.

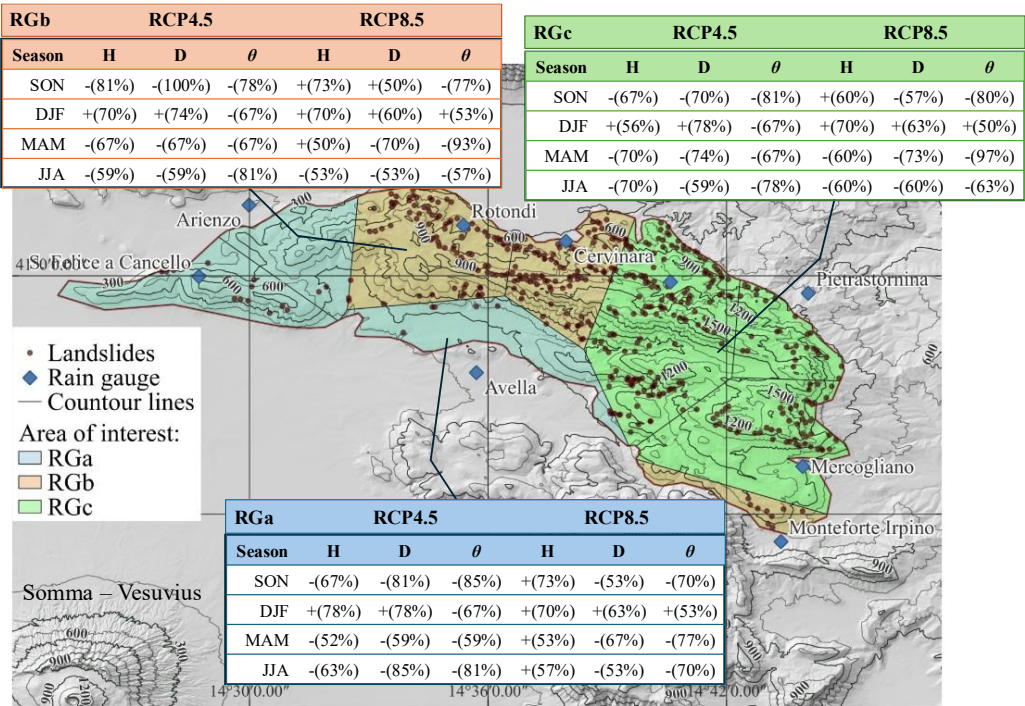


Figure 7. Subregional trend (positive “+” or negative “-”) and percentage of agreement (in brackets) of the ensemble members on rainfall (H), intensity (D) and antecedent volumetric water content (θ), according to RCP4.5 and RCP8.5 climate change scenarios.

3.2. Projected changes in landslide occurrence

The forthcoming analysis focuses on landslide-triggering rainfall events. Figure 8 shows the trends of temperature anomalies (ΔT) and the ensemble landslide frequency (λ_{LS}). The figure depicts the co-evolution of climate warming and slope instability under the RCP4.5 and RCP8.5 scenarios. The trend component of the CTRL scenario time series is also shown as a benchmark with current climate conditions.

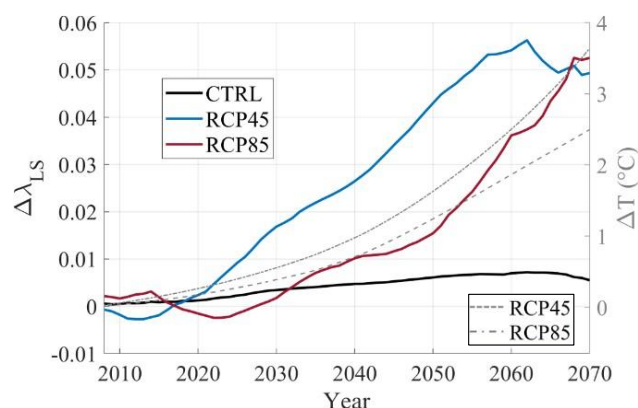


Figure 8. Anomalies on the trend component of the time series of temperature (ΔT) and landslide frequency trend ($\Delta \lambda_{LS}$) in the study period under RCP4.5 (blue) and RCP8.5 (red) scenarios, based on climate model ensemble simulations. Temperature change (ΔT) represents the anomaly relative to the 2006 baseline.

Figure 9 shows the trend component of λ_{LS} anomalies relative to the 2006 baseline for each climate change scenario, with dashed lines indicating the ensemble trend and solid lines the linear interpolation for SON (Figure 9(a)), DJF (Figure 9(b)), and MAM (Figure 9(c)). It seems clear that landslide frequency may increase specifically during DJF and MAM periods. In turn, Figure 10 presents the trends in anomalies of antecedent rainfall type (Figure 10(a, d, g)), triggering rainfall type (Figure 10(b, e, h)), and total rainfall amount (Figure 10(c, f, i)) during landslide-triggering events for the same periods. In both figures mean baseline values are reported on top left side as reference.

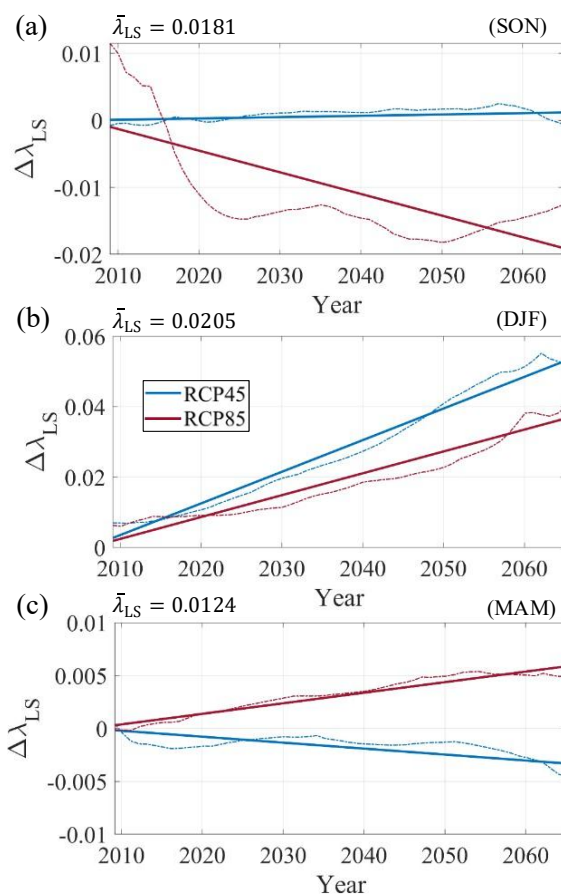


Figure 9. Anomalies on ensemble landslide frequency ($\Delta\lambda_{LS}$) for the three climate scenarios during the projected period. Panels (a–c) show seasonal trends for SON (a), DJF (b), and MAM (c), comparing RCP4.5 (blue) and RCP8.5 (red). Average landslide frequency ($\bar{\lambda}_{LS}$) at the start of the projected period is presented on top left side of each panel as reference.

From Figure 9 and Figure 10, it can be seen that under the RCP8.5 scenario there is an increase in λ_{LS} during DJF and MAM, driven by higher triggering rainfall events, while during DJF the RCP4.5 scenario shows an even stronger increase in λ_{LS} . In this case, the trend appears to coincide with an increase in antecedent rainfall type 3 and triggering rainfall type 1. Although explored in more detail later, the evolution of landslide occurrences, represented by the rate of change in λ_{LS} per year, naturally shows spatial variations related to both climate projections and rainfall spatial variability. However, the overall trend is preserved.

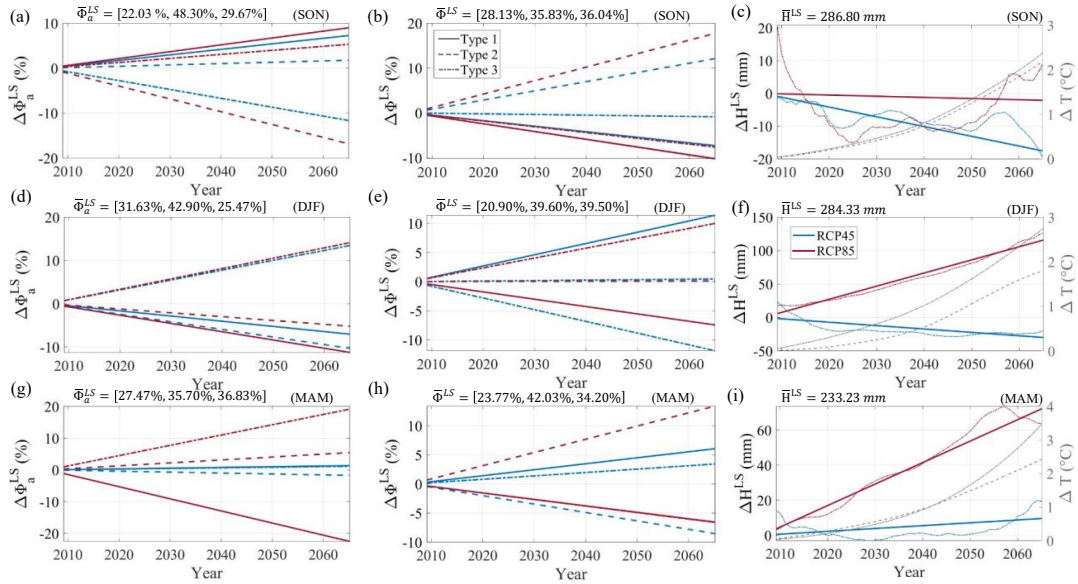


Figure 10. Trend component and linear interpolation of anomalies of: (a, d, g) antecedent rainfall type ($\Delta\Phi_a^{LS}$), (b, e, h) triggering rainfall type ($\Delta\Phi^{LS}$), and (c, f, i) total rainfall during landslide triggering events (ΔH^{LS}) in SON (a–c), DJF (d–f), and MAM (g–i). In (c), (f) and (i) dashed lines represent the trend component values, while solid lines are their linear interpolation. In all other cases lines represent only the linear interpolation of the trend for each rainfall type. Average magnitudes at the beginning of the period are presented on top-left side of each panel as a baseline reference for antecedent rainfall type $\Phi_a^{LS} = [\Phi_{a_1}^{LS}, \Phi_{a_2}^{LS}, \Phi_{a_3}^{LS}]$, triggering rainfall type $\Phi^{LS} = [\Phi_1^{LS}, \Phi_2^{LS}, \Phi_3^{LS}]$, and total triggering rainfall H^{LS} .

Table 1 shows the correlation coefficient between anomalies in trends of landslide frequency and antecedent rainfall types (Φ_a^{LS}), triggering rainfall types (Φ^{LS}) and total triggering rainfall (H^{LS}). Direct relationships are indicated by positive correlations in red cells. On the contrary, inverse relationships are indicated by negative correlations in blue cells. Clear direct relationships can be seen with ΔH^{LS} for RCP8.5 scenario in DJF and MAM. Interestingly, significant increases in landslide frequency coincide with positive correlations with increasing $\Delta\Phi_{a_3}^{LS}$ and $\Delta\Phi_1^{LS}$. This condition occurs in RCP4.5 scenario during the DJF period.

Table 1. Linear correlation coefficients from the correlations between anomalies in landslide frequency ($\Delta\lambda_{LS}$) and the anomalies in antecedent rainfall types ($\Delta\Phi_{a_{1,2,3}}^{LS}$), triggering rainfall types ($\Delta\Phi_{1,2,3}^{LS}$) and rainfall (ΔH) during triggering events for the DJF and MAM periods under RCP 4.5, RCP 8.5, and CTRL scenarios. Negative values (blue cells) indicate inverse relationships, while positive values (red cells) indicate direct relationships.

Scenario	Period	$\Delta\Phi_{a_1}^{LS}$	$\Delta\Phi_{a_2}^{LS}$	$\Delta\Phi_{a_3}^{LS}$	$\Delta\Phi_1^{LS}$	$\Delta\Phi_2^{LS}$	$\Delta\Phi_3^{LS}$	ΔH^{LS}
RCP4.5	DJF	-0.985	-0.529	0.985	0.975	-0.1	-0.985	-0.616
	MAM	-0.1	0.1	-0.13	-0.574	0.812	-0.781	-0.387
RCP8.5	DJF	-0.8	-0.86	0.917	-0.964	0.224	0.985	0.985
	MAM	-0.922	0.819	0.922	-0.9	0.917	-0.927	0.959



Figure 11 shows the anomalies in antecedent volumetric water content for landslide-triggering events (θ^{LS}) during the DJF and MAM periods. Specifically, while Figure 11(b) shows very subtle changes in θ^{LS} , Figure 11(a) indicates an increasing trend in θ^{LS} in DJF. This coincides with the absence of a clear correlation (or even an inverse relationship) between $\Delta\lambda_{LS}$ and ΔH^{LS} , particularly for RCP4.5 during DJF. Under such conditions, less rainfall may be required to trigger landslides as the antecedent wetting front just sets the landslide prone conditions when the triggering rainfall hit the slope.

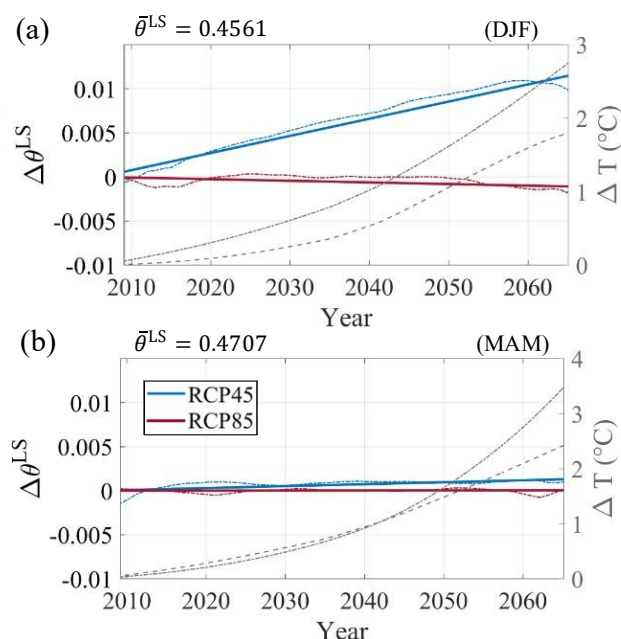


Figure 11. Anomalies of antecedent volumetric water content ($\Delta\theta^{LS}$) one hour before the onset of triggering rainfall events in DJF (a) and MAM (b).

3.2.1. Testing the significance of projected landslide changes

As the analyses shown above are tied to the variability expected from subregional spatial rainfall variations and climate modeling, Table 2 presents the results of an Analysis of Variance with Aligned Rank Transformed Data (ANOVA–ART) to statistically validate the findings. Using the number of landslides obtained from the simulations of each ensemble member for the period 2050–2070, the analysis considered three factors: the projected scenario (RCP4.5, RCP8.5 and CTRL), the location within the study area (RGa, RGb and RGc), and their interaction.



501 *Table 2. Analysis of Variance with Aligned Rank Transformed Data (ANOVA-ART) of the projected number of landslides between*
 502 *2050 and 2070, for each projected climate scenario and geographical position within the subregion. Levels of significance: (iii) α*
 503 *< 0.001 (ii) α < 0.01 (i) α < 0.05*

	F	<i>p</i> -value	Level of significance
Scenario	32.5861	< 0.001	(iii)
Position	5.1754	0.006319	(ii)
Scenario:Position	2.5393	0.040679	(i)

504

505 All factors show statistical significance, with the strongest effect confirming that the number of
 506 landslides toward the end of the period is primarily influenced by climate change scenarios. This
 507 is followed by location, which shows significant spatial differences within the study area. Finally,
 508 significant effects are also observed from the interaction between climate scenario and location.
 509 Given the statistical significance of the ANOVA–ART test, the Estimated Marginal Means
 510 (EMMs) method was applied as a post-hoc test to explore what are the climate scenarios and
 511 geographical positions showing sufficient statistical differences in triggering landslides at the end
 512 of the projected period. Table 3 shows the *p*-values associated with the test and the pairwise
 513 comparison between climate scenarios and different geographical positions characterized by the
 514 rain gauge group (i.e. RGa, RGb and RGc).

515 *Table 3. *p*-values from the statistical comparison of the projected number of landslides between 2050 and 2070 across different*
 516 *climate scenarios and geographical positions, using the Estimated Marginal Means (EMMs) method.*

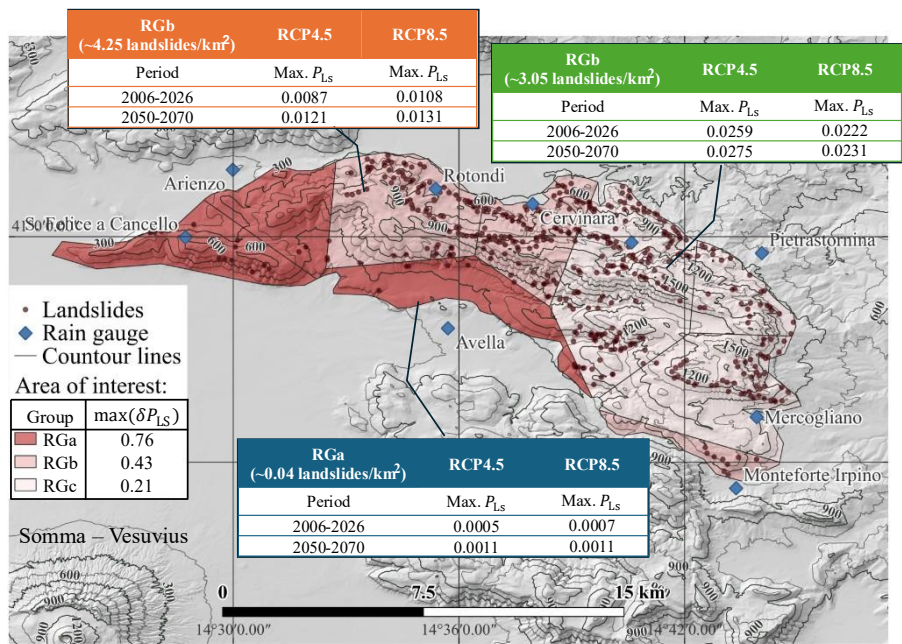
Comparison	RGa	RGb	RGc
RCP4.5 - RCP8.5	0.2567	0.2261	0.9617
RCP4.5 - CTRL	<.0001	<.0001	0.1644
RCP8.5 - CTRL	0.0007	<.0001	0.2667

517

518 The results from Table 3 indicate that scenarios considering climate change conditions (i.e. RCP4.5
 519 and RCP8.5) produce statistically significant differences in the number of landslides at the end of
 520 the studied period when compared with the CTRL scenario. However, the direct comparison
 521 between RCP4.5 and RCP8.5 does not reveal any statistically significant differences by the end of
 522 the projected period ($p > 0.22$ for all rain gauge groups).
 523 Interestingly, rainfall spatial variability plays a key role in some cases. For rain gauge groups RGa
 524 and RGb, both RCP4.5–CTRL and RCP8.5–CTRL comparisons yield highly significant results
 525 ($p < 0.001$), confirming that climate change conditions are likely to increase landslide occurrence
 526 in these regions. In contrast, RGc shows no statistically significant differences under either climate
 527 scenario ($p > 0.16$), suggesting lower sensitivity to projected climate change in that sub-region.



528 This pattern is consistent with the marginal landslide probability (P_{LS}) across the area for both
529 RCP4.5 and RCP8.5. The maximum P_{LS} is $\sim 7 \cdot 10^{-4}$ in RGa, ~ 0.01 in RGb, and ~ 0.023 in RGc.
530 As shown in Figure 12, RGa contains the fewest landslides (22 units), followed by RGb (207 units)
531 and RGc (238 units). This spatial pattern mirrors mean rainfall per event, as rain events in RGa
532 have on average ~ 22 mm/event, RGb ~ 30 mm/event, and RGc ~ 37 mm/event. However,
533 Figure 12 also highlights that the relative increase in landslide probability (δP_{LS}) between 2006–
534 2026 and 2050–2070 (considering both climate change scenarios) is highest in RGa and lowest in
535 RGc, indicating a proportionally stronger climate change signal in the less-affected western sector,
536 than in the eastern sector. Figure 12 displays the maximum shift in P_{LS} within each group.



537
538 *Figure 12. Spatial distribution of the maximum relative change in marginal probability of landslide occurrence (ΔP_{LS}) under the*
539 *climate change scenarios between 2006-2026 and 2050-2070.*

540

541 4. Discussion

542 Projected changes in rainfall and subsurface conditions indicate that, overall, the area is trending
543 toward drier soil conditions, particularly in autumn, spring and summer. These findings, consistent
544 with previous studies conducted at larger scales, suggest that even at local and subregional scales
545 the area tends towards aridity, but accompanied by significant rainfall variability driven by changes
546 in atmospheric conditions and its dynamics (Raffa et al., 2023; Rajczak and Schär, 2017). The



547 analysis of projected rainfall events at the nine rain gauge stations in the area clearly indicates that,
548 even if the rainfall proportion remains (i.e. Rainfall in RGc is greater than rainfall in RGb and
549 greater than rainfall in RGa), change signals may be stronger in some subregions than in others.
550 However, the resolution of most existing regional climate simulations in the analyzed ensemble
551 members is relatively coarse (~12.5 km), imposing a limitation to these results, particularly for
552 convective-scale rainstorms (~2–3 km), a capability that would be desirable for detailed studies
553 supporting landslide-scale hazard assessments.

554 Nonetheless, the assessment of climate change impacts on rainfall-triggered shallow landslides in
555 the area shows that, despite the trend toward drier conditions, a projected increase in landslide
556 occurrence is expected. In this study, future projections indicate a stronger increase in landslide
557 frequency under the RCP4.5 scenario compared to the RCP8.5 scenario. Similarly, a notable study
558 focusing on the nearby region of Calabria (southern Italy) projects a regional increase in the
559 number of landslides, with a stronger rise under RCP4.5 than under RCP8.5 for the period 2036–
560 2065 (Gariano et al., 2017).

561 As seen in the results, changes in landslide occurrence are closely linked to changes in rainfall
562 patterns. These conditions, which affect both triggering and antecedent rainfall events, drive
563 variations in meteorological landslide triggering mechanisms. Under RCP8.5 conditions,
564 landslide-triggering events are associated with a direct increase in triggering rainfall. In contrast,
565 under RCP4.5 conditions, landslide triggering is associated with a combination of increased
566 delayed (late-peak) antecedent rainfall, progressively leading to wetter antecedent soil conditions,
567 and advanced (early-peak) triggering rainfall patterns. These early-peak events produce higher
568 peak intensities earlier in the storm, reducing slope stability even during events with lower total
569 rainfall.

570 Regarding triggering conditions, clear changes are evident even in landslide records. Historical
571 data show a reduction in the average and maximum cumulative event rainfall required to initiate
572 landslides in nearby regions (Gariano et al., 2015). This suggests that slopes are becoming more
573 sensitive to instability, as shown in this study, due to progressively worsening predisposing
574 conditions. As a result, rainfall patterns appear to be evolving in a way that is more conducive to
575 triggering, regardless of total rainfall magnitude. Notably, these rainfall patterns are captured here
576 in the RCP4.5 ensemble.



577 A key role is played by antecedent soil moisture conditions, widely recognized as having a critical
578 impact on landslide triggering. Although changes in rainfall characteristics (such as patterns,
579 magnitudes, intensities, and event durations) have been demonstrated, critical antecedent soil
580 conditions are linked to relatively stable geomorphological settings and tend to remain constant
581 over time despite climate change. In practical terms, a large rainfall input is required to trigger a
582 landslide in relatively dry soil, whereas far less water is needed to trigger a landslide in already
583 saturated soil. Studies in southern Italy have shown that soil water content, relative to field
584 capacity, controls infiltration processes and landslide triggering mechanisms (Roman Quintero et
585 al., 2023, 2025). Preliminary analyses of rainfall intensity–duration thresholds for shallow
586 landslides in Basilicata (Southern Italy) further indicate that, in some cases, soil moisture exerts a
587 strong control on triggering, supporting this hypothesis (Lazzari et al., 2018). However,
588 establishing critical soil moisture conditions must rely on a physically based rationale, which is
589 more likely to be achieved in relatively well-characterized geological and morphological settings,
590 such as the study area presented here (Bezak et al., 2021; Marino et al., 2020b; Roman Quintero
591 et al., 2025).

592 Overall, the evidence points toward an increased future landslide risk in the study area, driven by
593 either a projected rise in triggering rainfall or changes in the rainfall conditions required for
594 triggering. However, recent studies using climate projections highlight uncertainties arising from
595 variability within projected ensemble members (Buonacera et al., 2025; Semnani et al., 2025). This
596 study shows that, despite ensemble variability, trends consistently indicate an increase in landslide
597 occurrence under future climate projections, supported by strong statistical evidence
598 demonstrating significant differences between current observed climate conditions (CTRL) and
599 climate change scenarios (RCP4.5 and RCP8.5) when analyzing the landslides occurring at the
600 end of the study period (2050–2070). These results also extend to rainfall spatial variability at the
601 subregional scale, with particularly pronounced changes in areas historically less affected by
602 landslides (i.e., RGa), but weaker signals in areas already prone to landslides and characterized by
603 the highest recorded and projected rainfall amounts in the region (i.e., RGc). However, although a
604 faster rise in landslide frequency is observed under RCP4.5 compared to RCP8.5, there is no
605 statistical evidence that this difference remains significant by the end of the study period.



5. Conclusions

We examined landslide occurrence in the Partenio Mountains (southern Italy) for 2006–2070 using EURO-CORDEX rainfall projections under RCP4.5 and RCP8.5, downscaled and bias-corrected with observations from nine rain gauges (2006–2023). Landslide triggering was analyzed with a calibrated 1D Richards infiltration model and stepwise stability assessment. The same procedure was applied to a synthetic rainfall dataset (CTRL) generated with a stochastic model reproducing observed rainfall conditions.

We conclude that projected rainfall and subsurface changes indicate a general trend toward drier soil conditions, particularly in autumn, spring, and summer, yet accompanied by significant spatial variability at the subregional scale. Despite this drying trend, landslide occurrence is projected to increase, with RCP4.5 showing a stronger rise in frequency than RCP8.5 up to mid-century, although differences between the scenarios are not statistically significant by 2050–2070, both scenarios showed significant differences with the CTRL scenario, representing currently observed conditions.

A further analysis of meteorological triggering mechanisms shows that, under RCP8.5, landslides are mainly associated with direct increases in total event rainfall. Under RCP4.5, however, the combination of wetter antecedent conditions, driven by delayed seasonal rainfall peaks, and earlier triggering rainfall peaks produces stronger destabilizing effects. Antecedent soil moisture therefore remains a critical control on landslide initiation, often exceeding the influence of total rainfall changes. As rainfall patterns shift, slopes become increasingly sensitive, with failures potentially triggered by smaller rainfall amounts due to elevated antecedent soil moisture. Consequently, projected changes in precipitation patterns cannot be always directly extrapolated to landslide occurrence: shifts in the return period of extreme rainfall events do not necessarily translate into equivalent changes in landslide return periods.

Taken together, these findings demonstrate that the interaction between climate change and slope hydrological processes can alter slope instability signal even under an overall drying trend, primarily through shifts in rainfall timing and intensity that alter antecedent soil conditions, specifically in extreme events. The consistent increase in projected landslide occurrence across scenarios and subregions highlights the sensitivity of the landscape to evolving hydrometeorological dynamics. This study therefore provides quantitative and process-based evidence that future landslide hazard may intensify not simply because of how much it rains, but



637 because of *when* and *how* rainfall occurs. The results align with recent investigations in nearby
638 regions, strengthening the emerging consensus that changes in rainfall patterning, rather than totals
639 alone, will play a decisive role in shaping slope stability under future climate conditions. These
640 insights underscore the need for climate-resilient risk management strategies that explicitly
641 account for rainfall pattern variability and antecedent moisture dynamics in landslide-prone areas.



642 **Competing interests**

643 At least one of the (co-)authors is a member of the editorial board of Natural Hazards and Earth
 644 System Sciences.

645 **Code availability**

646 The code used for the bias correction and downscaling analysis is openly available on Zenodo:
 647 *Daniel C. Roman Q. (2025). dromanq/Bias-Correction-QME: Bias-Correction-QME v1.0.0 —*
 648 *Downscaling & Bias Correction of Precipitation Model Data. Zenodo.*
 649 <https://doi.org/10.5281/zenodo.17644202> (Roman Quintero, 2025)

650 **Author contributions**

651 All authors designed the research. RE and DCRQ developed the modelling framework, performed
 652 the bias correction, and carried out the hydrological and slope-stability simulations. All authors
 653 analyzed the results and DCRQ prepared the figures. TB and RG supervised the study. DCRQ
 654 wrote the initial manuscript draft. RE, TB, and RG reviewed and edited the manuscript.

655 **Financial support**

656 This study was carried out within the RETURN Extended Partnership and received funding from
 657 the European Union Next-GenerationEU (National Recovery and Resilience Plan – NRRP,
 658 Mission 4, Component 2, Investment 1.3 – D.D. 1243 2/8/2022, PE00000005).

659 **6. References**

- 660 Avino, A., Cimorelli, L., Furcolo, P., Noto, L. V., Pelosi, A., Pianese, D., Villani, P., and Manfreda,
 661 S.: Are rainfall extremes increasing in southern Italy?, *J Hydrol (Amst)*, 631, 130684,
 662 <https://doi.org/10.1016/J.JHYDROL.2024.130684>, 2024.
- 663 Bezak, N., Jemec Auflič, M., and Mikoš, M.: Reanalysis of soil moisture used for rainfall
 664 thresholds for rainfall-induced landslides: The Italian case study, *Water (Switzerland)*, 13,
 665 <https://doi.org/10.3390/w13141977>, 2021.
- 666 Bogaard, T. and Greco, R.: *Landslide hydrology: from hydrology to pore pressure*, Wiley
 667 *Interdisciplinary Reviews: Water*, 3, 439–459, <https://doi.org/10.1002/wat2.1126>, 2016.
- 668 Bozzolan, E., Holcombe, E., Pianosi, F., and Wagener, T.: Synthetic libraries of urban landslide
 669 simulations to identify slope failure hotspots and drivers across spatial scales and landscapes,
 670 *Landslides*, 22, 637–654, <https://doi.org/10.1007/s10346-024-02327-4>, 2025.
- 671 Bucchignani, E., Montesarchio, M., Zollo, A. L., and Mercogliano, P.: High-resolution climate
 672 simulations with COSMO-CLM over Italy: performance evaluation and climate projections for the



673 21st century, *International Journal of Climatology*, 36, 735–756,
 674 <https://doi.org/10.1002/JOC.4379>, 2016.

675 Buonacera, G., Palazzolo, N., Cancelliere, A., and Peres, D. J.: Deriving Future Rainfall Depth-
 676 Duration-Frequency Curves from Hourly Regional Climate Projections and Simple Scaling in
 677 Sicily, *Water Resources Management*, 1–17, <https://doi.org/10.1007/S11269-025-04219-1>, 2025.

678 Capozzi, V., Rocco, A., Annella, C., Cretella, V., Fusco, G., and Budillon, G.: Signals of change in
 679 the Campania region rainfall regime: An analysis of extreme precipitation indices (2002–2021),
 680 *Meteorological Applications*, 30, e2168, <https://doi.org/10.1002/MET.2168>, 2023.

681 Celico, F., Naclerio, G., Bucci, A., Nerone, V., Capuano, P., Carcione, M., Allocca, V., and Celico,
 682 P.: Influence of pyroclastic soil on epikarst formation: a test study in southern Italy, *Terra Nova*,
 683 22, 110–115, <https://doi.org/10.1111/J.1365-3121.2009.00923.X>, 2010.

684 Cowpertwait, P. S. P., O’Connell, P. E., Metcalfe, A. V., and Mawdsley, J. A.: Stochastic point
 685 process modelling of rainfall. I. Single-site fitting and validation, *J Hydrol (Amst)*,
 686 [https://doi.org/10.1016/S0022-1694\(96\)80004-7](https://doi.org/10.1016/S0022-1694(96)80004-7), 1996.

687 Crozier, M. J.: Deciphering the effect of climate change on landslide activity: A review,
 688 *Geomorphology*, 124, 260–267, <https://doi.org/10.1016/J.GEOMORPH.2010.04.009>, 2010.

689 Davie, J. C. S., Falloon, P. D., Kahana, R., Dankers, R., Betts, R., Portmann, F. T., Wisser, D.,
 690 Clark, D. B., Ito, A., Masaki, Y., Nishina, K., Fekete, B., Tessler, Z., Wada, Y., Liu, X., Tang, Q.,
 691 Hagemann, S., Stacke, T., Pavlick, R., Schaphoff, S., Gosling, S. N., Franssen, W., and Arnell, N.:
 692 Comparing projections of future changes in runoff from hydrological and biome models in ISI-
 693 MIP, *Earth System Dynamics*, 4, 359–374, <https://doi.org/10.5194/ESD-4-359-2013>, 2013.

694 D’Odorico, P., Fagherazzi, S., and Rigon, R.: Potential for landsliding: Dependence on hyetograph
 695 characteristics, *J Geophys Res Earth Surf*, 110, 1007, <https://doi.org/10.1029/2004JF000127>,
 696 2005.

697 Dowdy, A.: A bias correction method designed for weather and climate extremes, Australian
 698 Bureau of Meteorology, 63 pp., 2023.

699 Ehret, U., Zehe, E., Wulfmeyer, V., Warrach-Sagi, K., and Liebert, J.: HESS Opinions “Should we
 700 apply bias correction to global and regional climate model data?,” *Hydrol Earth Syst Sci*, 16, 3391–
 701 3404, <https://doi.org/10.5194/HESS-16-3391-2012>, 2012.



- 702 Erdfelder, E., FAul, F., Buchner, A., and Lang, A. G.: Statistical power analyses using G*Power
703 3.1: Tests for correlation and regression analyses, *Behav Res Methods*, 41, 1149–1160,
704 <https://doi.org/10.3758/BRM.41.4.1149>, 2009.
- 705 Fang, Z., Wang, Y., van Westen, C., and Lombardo, L.: Space-time modeling of landslide size by
706 combining static, dynamic, and unobserved spatiotemporal factors, *Catena (Amst)*, 240, 107989,
707 <https://doi.org/10.1016/J.CATENA.2024.107989>, 2024.
- 708 Gariano, S. L. and Guzzetti, F.: Landslides in a changing climate, *Earth Sci Rev*, 162, 227–252,
709 <https://doi.org/10.1016/J.EARSCIREV.2016.08.011>, 2016.
- 710 Gariano, S. L., Petrucci, O., and Guzzetti, F.: Changes in the occurrence of rainfall-induced
711 landslides in Calabria, southern Italy, in the 20th century, *Natural Hazards and Earth System*
712 *Sciences*, 15, 2313–2330, <https://doi.org/10.5194/NHESS-15-2313-2015>, 2015.
- 713 Gariano, S. L., Rianna, G., Petrucci, O., and Guzzetti, F.: Assessing future changes in the
714 occurrence of rainfall-induced landslides at a regional scale, *Science of the Total Environment*,
715 596–597, 417–426, <https://doi.org/10.1016/j.scitotenv.2017.03.103>, 2017.
- 716 Golyandina, N. and Zhigljavsky, A.: *Singular Spectrum Analysis for Time Series*, Springer Berlin
717 Heidelberg, Berlin, Heidelberg, <https://doi.org/10.1007/978-3-642-34913-3>, 2013.
- 718 Greco, R., Comegna, L., Damiano, E., Guida, A., Olivares, L., and Picarelli, L.: Hydrological
719 modelling of a slope covered with shallow pyroclastic deposits from field monitoring data, *Hydrol*
720 *Earth Syst Sci*, 17, 4001–4013, <https://doi.org/10.5194/hess-17-4001-2013>, 2013.
- 721 Greco, R., Marino, P., Santonastaso, G. F., and Damiano, E.: Interaction between perched epikarst
722 aquifer and unsaturated soil cover in the initiation of shallow landslides in pyroclastic soils, *Water*
723 *(Switzerland)*, 10, <https://doi.org/10.3390/w10070948>, 2018.
- 724 Greco, R., Comegna, L., Damiano, E., Marino, P., Olivares, L., and Santonastaso, G. F.: Recurrent
725 rainfall-induced landslides on the slopes with pyroclastic cover of Partenio Mountains (Campania,
726 Italy): Comparison of 1999 and 2019 events, *Eng Geol*, 288, 106160,
727 <https://doi.org/10.1016/j.enggeo.2021.106160>, 2021.
- 728 Greco, R., Marino, P., and Bogaard, T. A.: Recent advancements of landslide hydrology, *Wiley*
729 *Interdisciplinary Reviews: Water*, e1675, <https://doi.org/10.1002/WAT2.1675>, 2023.
- 730 Gründemann, G. J., van de Giesen, N., Brunner, L., and van der Ent, R.: Rarest rainfall events will
731 see the greatest relative increase in magnitude under future climate change, *Commun Earth*
732 *Environ*, 3, 1–9, <https://doi.org/10.1038/S43247-022-00558-8>, 2022.



- 733 Iadanza, C., Trigila, A., Starace, P., Dragoni, A., Biondo, T., and Roccisano, M.: IdroGEO: A
 734 collaborative web mapping application based on REST API services and open data on landslides
 735 and floods in Italy, *ISPRS Int J Geoinf*, 10, <https://doi.org/10.3390/IJGI10020089>, 2021.
- 736 Jacob, D., Petersen, J., Eggert, B., Alias, A., Christensen, O. B., Bouwer, L. M., Braun, A., Colette,
 737 A., Déqué, M., Georgievski, G., Georgopoulou, E., Gobiet, A., Menut, L., Nikulin, G., Haensler,
 738 A., Hempelmann, N., Jones, C., Keuler, K., Kovats, S., Kröner, N., Kotlarski, S., Kriegsmann, A.,
 739 Martin, E., van Meijgaard, E., Moseley, C., Pfeifer, S., Preuschmann, S., Radermacher, C., Radtke,
 740 K., Rechid, D., Rounsevell, M., Samuelsson, P., Somot, S., Soussana, J. F., Teichmann, C.,
 741 Valentini, R., Vautard, R., Weber, B., and Yiou, P.: EURO-CORDEX: New high-resolution climate
 742 change projections for European impact research, *Reg Environ Change*, 14, 563–578,
 743 <https://doi.org/10.1007/s10113-013-0499-2>, 2014.
- 744 Kim, Y., Evans, J. P., and Sharma, A.: Multivariate bias correction of regional climate model
 745 boundary conditions, *Climate Dynamics* 2023 61:7, 61, 3253–3269,
 746 <https://doi.org/10.1007/S00382-023-06718-6>, 2023.
- 747 Lazzari, M., Piccarreta, M., and Manfreda, S.: The role of antecedent soil moisture conditions on
 748 rainfall-triggered shallow landslides, <https://doi.org/10.5194/NHESS-2018-371>, 2018.
- 749 Lenth, R. V.: Estimated Marginal Means, aka Least-Squares Means,
 750 <https://doi.org/10.1080/00031305.1980.10483031>, 2025.
- 751 Marino, P., Comegna, L., Damiano, E., Olivares, L., and Greco, R.: Monitoring the hydrological
 752 balance of a landslide-prone slope covered by pyroclastic deposits over limestone fractured
 753 bedrock, *Water (Switzerland)*, 12, <https://doi.org/10.3390/w12123309>, 2020a.
- 754 Marino, P., Peres, D. J., Cancelliere, A., Greco, R., and Bogaard, T.: Soil moisture information can
 755 improve shallow landslide forecasting using the hydrometeorological threshold approach,
 756 *Landslides*, 17, 2041–2054, <https://doi.org/10.1007/s10346-020-01420-8>, 2020b.
- 757 Marino, P., Santonastaso, G. F., Fan, X., and Greco, R.: Prediction of shallow landslides in
 758 pyroclastic-covered slopes by coupled modeling of unsaturated and saturated groundwater flow,
 759 *Landslides*, 18, 31–41, <https://doi.org/10.1007/s10346-020-01484-6>, 2021.
- 760 Moss, R. H., Edmonds, J. A., Hibbard, K. A., Manning, M. R., Rose, S. K., Van Vuuren, D. P.,
 761 Carter, T. R., Emori, S., Kainuma, M., Kram, T., Meehl, G. A., Mitchell, J. F. B., Nakicenovic, N.,
 762 Riahi, K., Smith, S. J., Stouffer, R. J., Thomson, A. M., Weyant, J. P., and Wilbanks, T. J.: The next



763 generation of scenarios for climate change research and assessment, *Nature*, 463, 747–756,
 764 <https://doi.org/10.1038/NATURE08823>, 2010.

765 Neyman, J. and Scott, E. L.: Statistical Approach to Problems of Cosmology, *Journal of the Royal*
 766 *Statistical Society: Series B (Methodological)*, [https://doi.org/10.1111/j.2517-](https://doi.org/10.1111/j.2517-6161.1958.tb00272.x)
 767 [6161.1958.tb00272.x](https://doi.org/10.1111/j.2517-6161.1958.tb00272.x), 1958.

768 Peres, D. J. and Cancelliere, A.: Derivation and evaluation of landslide-triggering thresholds by a
 769 Monte Carlo approach, *Hydrol Earth Syst Sci*, 18, 4913–4931, [https://doi.org/10.5194/HESS-18-](https://doi.org/10.5194/HESS-18-4913-2014)
 770 [4913-2014](https://doi.org/10.5194/HESS-18-4913-2014), 2014.

771 Peres, D. J. and Cancelliere, A.: Estimating return period of landslide triggering by Monte Carlo
 772 simulation, *J Hydrol (Amst)*, 541, 256–271, <https://doi.org/10.1016/J.JHYDROL.2016.03.036>,
 773 2016.

774 Peter, J., Vogel, E., Sharples, W., Bende-Michl, U., Wilson, L., Hope, P., Dowdy, A., Kociuba, G.,
 775 Srikanthan, S., Duong, V. C., Roussis, J., Matic, V., Khan, Z., Oke, A., Turner, M., Baron-Hay, S.,
 776 Johnson, F., Mehrotra, R., Sharma, A., Thatcher, M., Azarvinand, A., Thomas, S., Boschhat, G.,
 777 Donnelly, C., and Argent, R.: Continental-scale bias-corrected climate and hydrological
 778 projections for Australia, *Geosci Model Dev*, 17, 2755–2781, [https://doi.org/10.5194/GMD-17-](https://doi.org/10.5194/GMD-17-2755-2024)
 779 [2755-2024](https://doi.org/10.5194/GMD-17-2755-2024), 2024.

780 Picarelli, L., Evangelista, A., Rolandi, G., and Paone, A.: Mechanical properties of pyroclastic soils
 781 in Campania Region. *Proc. 2nd Int. Work. on Characterisation and Engineering Properties of*
 782 *Natural Soils The 5th Italian Workshop on Landslides-IWL 2018 View project Structural*
 783 *monitoring and sensing View project*, 2006.

784 Picarelli, L., Olivares, L., Lampitiello, S., Darban, R., and Damiano, E.: The undrained behaviour
 785 of an air-fall volcanic ash, *Geosciences (Switzerland)*, 10,
 786 <https://doi.org/10.3390/geosciences10020060>, 2020.

787 Raffa, M., Adinolfi, M., Reder, A., Marras, G. F., Mancini, M., Scipione, G., Santini, M., and
 788 Mercogliano, P.: Very High Resolution Projections over Italy under different CMIP5 IPCC
 789 scenarios, *Scientific Data* 2023 10:1, 10, 1–13, <https://doi.org/10.1038/s41597-023-02144-9>,
 790 2023.

791 Rajczak, J. and Schär, C.: Projections of Future Precipitation Extremes Over Europe: A
 792 Multimodel Assessment of Climate Simulations, *Journal of Geophysical Research: Atmospheres*,
 793 122, 10,773–10,800, <https://doi.org/10.1002/2017JD027176>, 2017.



- 794 Rodriguez-Iturbe, I., Febres De Power, B., and Valdes, J. B.: Rectangular pulses point process
795 models for rainfall: Analysis of empirical data, *Journal of Geophysical Research: Atmospheres*,
796 92, 9645–9656, <https://doi.org/10.1029/JD092ID08P09645>, 1987a.
- 797 Rodriguez-Iturbe, I., Febres De Power, B., and Valdes, J. B.: Rectangular pulses point process
798 models for rainfall: analysis of empirical data, *J Geophys Res*,
799 <https://doi.org/10.1029/JD092iD08p09645>, 1987b.
- 800 Roman Quintero, D. C.: dromanq/Bias-Correction-QME: Bias-Correction-QME v1.0.0 —
801 Downscaling & Bias Correction of Precipitation Model Data ,
802 <https://doi.org/10.5281/zenodo.17644202>, November 2025.
- 803 Roman Quintero, D. C., Marino, P., Santonastaso, G. F., and Greco, R.: Understanding hydrologic
804 controls of sloping soil response to precipitation through machine learning analysis applied to
805 synthetic data, *Hydrol Earth Syst Sci*, 27, 4151–4172, [https://doi.org/10.5194/HESS-27-4151-](https://doi.org/10.5194/HESS-27-4151-2023)
806 2023, 2023.
- 807 Roman Quintero, D. C., Marino, P., Abdullah, A., Santonastaso, G. F., and Greco, R.: Large-scale
808 assessment of rainfall-induced landslide hazard based on hydrometeorological information:
809 application to Partenio Massif (Italy), *EGUsphere*, 1–29, [https://doi.org/10.5194/EGUSPHERE-](https://doi.org/10.5194/EGUSPHERE-2024-2329)
810 2024-2329, 2024a.
- 811 Roman Quintero, D. C., Damiano, E., Olivares, L., and Greco, R.: Mechanical and hydraulic
812 properties of unsaturated layered pyroclastic ashes in landslide-prone areas of Campania (Italy),
813 *Bulletin of Engineering Geology and the Environment* 2024 83:7, 83, 1–12,
814 <https://doi.org/10.1007/S10064-024-03783-X>, 2024b.
- 815 Roman Quintero, D. C., Marino, P., Abdullah, A., Santonastaso, G. F., and Greco, R.: Large-scale
816 assessment of rainfall-induced landslide hazard based on hydrometeorological information:
817 application to Partenio Massif (Italy), *Natural Hazards and Earth System Sciences*, 25, 2679–2698,
818 <https://doi.org/10.5194/NHESS-25-2679-2025>, 2025.
- 819 Searle, S. R., Speed, F. M., and Milliken, G. A.: Population marginal means in the linear model:
820 An alternative to least squares means, *American Statistician*, 34, 216–221,
821 <https://doi.org/10.1080/00031305.1980.10483031>, 1980.
- 822 Semnani, S. J., Han, Y., Bonfils, C. J., and White, J. A.: Assessing the impact of climate change on
823 rainfall-triggered landslides: a case study in California, *Landslides*, 22, 1707–1724,
824 <https://doi.org/10.1007/S10346-024-02428-0>, 2025.



- 825 Del Soldato, M., Pazzi, V., Segoni, S., De Vita, P., Tofani, V., and Moretti, S.: Spatial modeling of
 826 pyroclastic cover deposit thickness (depth to bedrock) in peri-volcanic areas of Campania
 827 (southern Italy), *Earth Surf Process Landf*, 43, 1757–1767, <https://doi.org/10.1002/ESP.4350>,
 828 2018.
- 829 Stoffel, M., Tiranti, D., and Huggel, C.: Climate change impacts on mass movements - Case studies
 830 from the European Alps, *Science of the Total Environment*, 493, 1255–1266,
 831 <https://doi.org/10.1016/j.scitotenv.2014.02.102>, 2014.
- 832 Taylor, K. E., Stouffer, R. J., and Meehl, G. A.: An overview of CMIP5 and the experiment design,
 833 <https://doi.org/10.1175/BAMS-D-11-00094.1>, April 2012.
- 834 Teutschbein, C. and Seibert, J.: Bias correction of regional climate model simulations for
 835 hydrological climate-change impact studies: Review and evaluation of different methods, *J Hydrol*
 836 (Amst), 456–457, 12–29, <https://doi.org/10.1016/J.JHYDROL.2012.05.052>, 2012.
- 837 De Vita, P. and Nappi, M.: Regional distribution of ash-fall pyroclastic soils for landslide
 838 susceptibility assessment, *Landslide Science and Practice: Spatial Analysis and Modelling*, 3, 103–
 839 109, https://doi.org/10.1007/978-3-642-31310-3_15, 2013.
- 840 Vogel, E., Johnson, F., Marshall, L., Bende-Michl, U., Wilson, L., Peter, J. R., Wasko, C.,
 841 Srikanthan, S., Sharples, W., Dowdy, A., Hope, P., Khan, Z., Mehrotra, R., Sharma, A., Matic, V.,
 842 Oke, A., Turner, M., Thomas, S., Donnelly, C., and Duong, V. C.: An evaluation framework for
 843 downscaling and bias correction in climate change impact studies, *J Hydrol (Amst)*, 622, 129693,
 844 <https://doi.org/10.1016/J.JHYDROL.2023.129693>, 2023.
- 845 van Vuuren, D. P., Edmonds, J., Kainuma, M., Riahi, K., Thomson, A., Hibbard, K., Hurtt, G. C.,
 846 Kram, T., Krey, V., Lamarque, J. F., Masui, T., Meinshausen, M., Nakicenovic, N., Smith, S. J.,
 847 and Rose, S. K.: The representative concentration pathways: An overview, *Clim Change*, 109, 5–
 848 31, <https://doi.org/10.1007/S10584-011-0148-Z>, 2011.
- 849 Williams, P. W.: The role of the epikarst in karst and cave hydrogeology: a review, *Int J Speleol*,
 850 37, 1–10, <https://doi.org/10.5038/1827-806X.37.1.1>, 2008.
- 851 Wobbrock, J. O., Findlater, L., Gergle, D., and Higgins, J. J.: The Aligned Rank Transform for
 852 Nonparametric Factorial Analyses Using Only ANOVA Procedures, 2011.
- 853 Wu, S. J., Yang, J. C., and Tung, Y. K.: Identification and stochastic generation of representative
 854 rainfall temporal patterns in Hong Kong territory, *Stochastic Environmental Research and Risk*
 855 *Assessment*, 20, 171–183, <https://doi.org/10.1007/S00477-005-0245-5>, 2006.